GeoStorage

Vol. 2, No. 1, p. 27-39, 2026

Research article

Investigating Fracture Activation and CO_2 Migration in Layered Shale Caprock: A Phase-field Approach

Yanji Fu[1], Shaobo Qiao[1], Huimin Wang[1], Jia Liu[2], Zhihan Li[1,3], Jinchang Sheng[1]*

[1] *College of Water Conservancy and Hydropower Engineering, Hohai University, Nanjing 210098, China*
[2] *State Key Laboratory of Eco-hydraulics in Northwest Arid Region, Xi'an University of Technology, Xi'an 710048, China*
[3] *College of Urban and Rural Construction, Shanxi Agricultural University, Jinzhong 030801, China*

Keywords:
Layered shale caprock
weak interlayers
phase field method
CO_2 pressure
sealing efficiency

Cited as:
Fu YJ, Qiao SB, Wang HM, et al. 2026. Investigating Fracture Activation and CO_2 Migration in Layered Shale Caprock: A Phase-field Approach. *GeoStorage*, 2(1), 27-39.
https://doi.org/10.46690/gs.2026.01.03

Abstract:
Although low-permeability layered shale has been regarded as a natural barrier for CO_2 leakage, the accumulation of CO_2 beneath the caprock may reactivate original fractures and even connect interlayers. This behavior significantly threatens the sealing integrity of layered shale caprock. Therefore, our study defines the "weak interlayer" as thin layer with low mechanical strength. Subsequently, we developed a phase-field framework to investigate initial fracture activation, fracture extension and deflection, and pore pressure dispersion within layers. The accuracy of the proposed model was validated through tensile experiments on 2D notched plates and hydraulic fracturing experiments conducted on specimens containing circular perforations. Simulation results indicate that while the increase in in-situ stress raises the threshold for activating original fractures, their extension tends to be along the vertical direction. Similarly, a reduction in horizontal stress accelerates the fracture extension in the vertical direction. Lowering the permeability of "weak interlayer" hinders lateral dispersion of CO_2 pressure, promoting vertical migration through the caprock. Conversely, reducing the injection rate allows easier lateral migration of CO_2 along "weak interlayer", thereby improving sealing efficiency. These findings provide practical guidance for site selection in geological CO_2 geological sequestration, insights into fracture activation, propagation, and connectivity, and an assessment of layered shale caprock sealing efficiency.

1 Introduction

CO_2 capture and storage (CCS) has been identified as one of the most feasible approaches for reducing atmospheric CO_2 concentrations (IPCC, 2014, 2007). Ensuring long-term secure storage of CO_2 critically depends on the integrity of the overlying low-permeability caprock. Initially, the caprock contains few original fractures or these fractures remain in a closed state, resulting in extremely low permeability. Consequently, the caprock remains relatively stable before CO_2 injection. The primary pathways for CO_2 leakage include: (i) diffusion of dissolved CO_2 across the caprock, (ii) CO_2 breakthrough via interconnected pore spaces, and (iii) CO_2 leakage through faults, fractures, and wellbores (Kaldi et al., 2013). Among these mechanisms, leakage through faults and fractures is significantly more rapid and severe (Newell and Martinez, 2020). Therefore, predicting fracture propagation within the caprock is crucial for ensuring CO_2 sealing efficiency.

CO_2 in the reservoir gradually accumulates beneath the caprock due to buoyancy forces, generating high pressure (Onoja et al., 2019; Wang et al., 2015; Wang and Peng, 2014). This elevated pressure can lead to ground uplift, increasing the risk of caprock failure (Lee et al., 2013). For example, in the In Salah CO_2 geological sequestration project, an uplift of approximately 5 mm per year was observed (Rutqvist et al., 2010). Furthermore, when the pressure of CO_2 accumulated beneath the caprock exceeds the tensile strength of the caprock, it may reactivate pre-existing fractures or induce new fractures, which become major pathways for CO_2 leakage (Lee et al.,

* Corresponding author.
E-mail address: 220202010002@hhu.edu.cn (Fu YJ); 878958976@qq.com (Qiao SB); huimin.wang@hhu.edu.cn (Wang HM); jliu@xaut.edu.cn (Liu J); sxnydxlzh@163.com (Li ZH); sh901@sina.com (Sheng JC)

Received Dec. 12, 2025; revised Dec. 28, 2025; accepted Jan. 8, 2026; available online Jan. 22, 2026.

Yandy Scientific Press

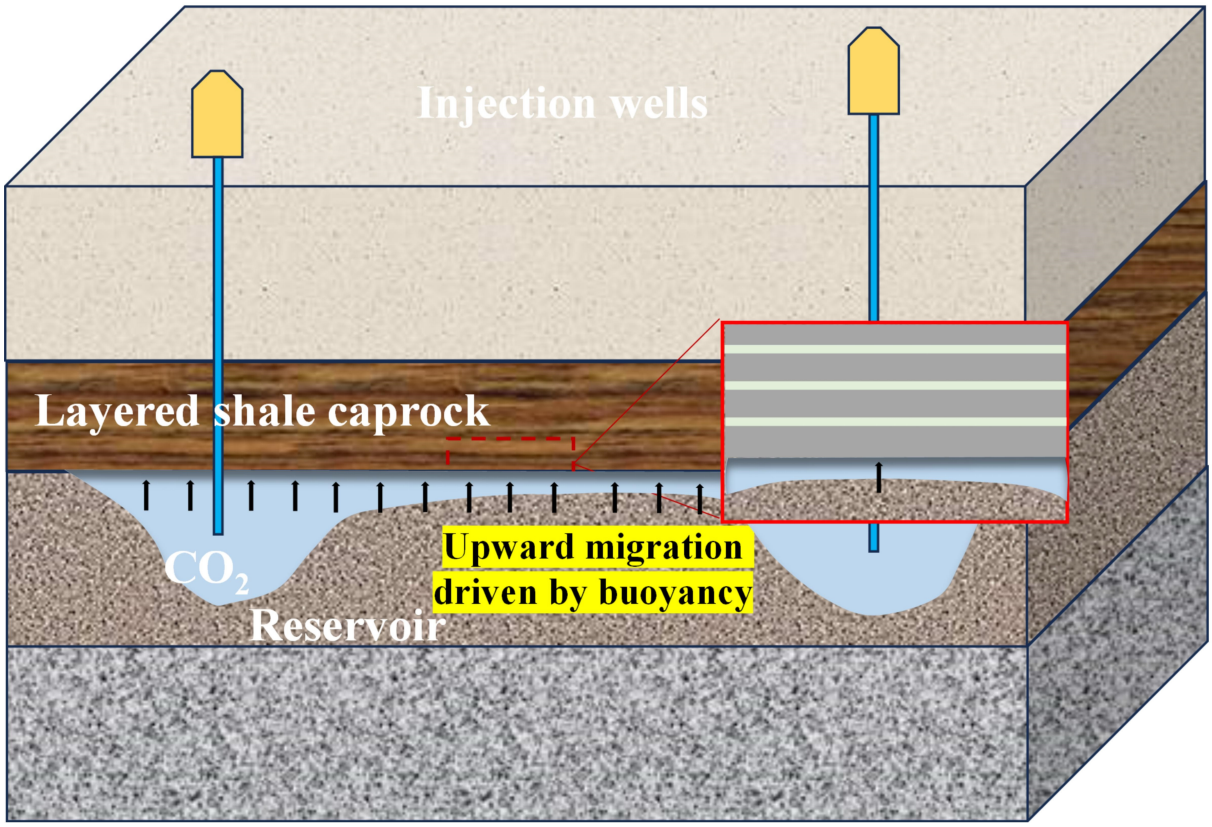

Fig. 1 Schematic diagram of CO_2 penetration into layered shale caprock

2013). Vilarrasa et al. suggested that the boundaries between the caprock and the reservoir are low-permeability interfaces (Vilarrasa et al., 2010, 2011). During the initial stage of CO_2 penetration into the caprock, CO_2 accumulates at the lower part of the caprock, leading to a sharp increase in fluid pressure, at which point the risk of caprock failure is the highest. Chen et al. suggested that an increase in caprock burial depth significantly raises the fracture pressure of the caprock, but the increment in pore pressure and the uplift displacement of the formation do not change notably (Chen et al., 2024). Therefore, the risk of caprock fracture and leakage also increases accordingly. Yamamoto et al. indicated that CO_2 penetration into the caprock results in a significant increase in internal pressure accumulation and deformation, which increases the deviatoric stress and markedly raises the risk of caprock fracture (Yamamoto et al., 2013). A higher injection rate exacerbates this effect, while reducing the injection rate enhances the sealing security of the caprock.

The aforementioned studies have discussed the impact of external conditions on the sealing integrity of the caprock. Layered shale caprock, as a type of sedimentary rock, inherently contains high-permeability "weak interlayer" due to its formation mechanism. Existing research has shown that layered shale caprock with "weak interlayer" offers significant advantages in terms of sealing security. However, under extreme conditions, layered shale caprock containing "weak interlayer" may still develop vertical fractures, leading to CO_2 leakage. Therefore, predicting the fracture propagation path in layered shale caprock containing "weak interlayer" is crucial for CO_2 geological sequestration.

Currently, the phase-field method has shown significant advantages in predicting fracture growth in layered rocks. Liu et al. used interpolation functions within the phase-field framework to characterize the parameter differences between shale layers and the matrix (Liu et al., 2019). While this method partially reveals the impact of layering on rock fracturing, it lacks theoretical support and is imprecise regarding the given width of the bedding plane. To address these issues, Liu et al. proposed two improvements to the model: (1) Introducing low-dimensional interface elements and tangential derivative variables to describe the phase-field evolution at interfaces, discretizing the low-dimensional interface and the rock matrix, and verifying models with varying bonding degrees in layered rock fractures (Liu et al., 2021). (2)Assuming the formation consists of elastic thin layers with independent mechanical parameters, discretizing these layers along the rock matrix using low-dimensional interface elements within the finite element framework (Liu et al., 2022). Subsequently, Zeng et al. applied this method to study hydraulic fracture propagation in multilayer formations, analyzing the effects of various factors on fracture propagation behaviors (Zeng et al., 2023). In summary, the phase-field method is well-suited for predicting fracture behaviors in layered rocks. However, most current studies on fracture propagation in multilayer formations focus on hydraulic fracturing and often overlook the effects of fluid properties within the formation. During CO_2 geological sequestration, CO_2 is stored in a supercritical state, which has lower density and viscosity compared to water, and its physical properties

change significantly as it migrates upward (Wang and Wang, 2018; Span and Wagner, 1996). Moreover, most models only consider mechanical property differences between the "weak interlayer" and the matrix. In reality, the permeability of the "weak interlayer" is one to two orders of magnitude higher than that of the matrix, which plays a critical role in fracture propagation in layered shale caprocks. The fracture propagation pattern of CO_2 in layered shale caprocks remains unclear.

This study presents a phase-field model to investigate initial fracture activation, fracture extension and deflection, and pore pressure diffusion during CO_2 penetration into the layered shale caprock. It also analyzes the effects of in-situ stress, "weak interlayer" permeability, and injection rate on these processes. The rest of the study is organized as follows: Section 2 presents the derivation process of the variational phase-field theory for interfacial fracture. Section 3 provides model validation. Section 4 presents a detailed numerical simulation exploring the sensitivity of model parameters. Finally, Section 5 presents the critical conclusions.

2 Formulation of governing equations

2.1 Energy functional

The phase-field method was initially derived from Griffith's theory and the variational principle (Francfort and Marigo, 1998). For CO_2 in layered shale caprocks, the energy functional over the entire computational domain consists of elastic energy, fracture surface energy, pressure dissipation energy, external work, and the influence of fluid pressure in porous media (Lee et al., 2016; Mikelić et al., 2015; Zhou et al., 2018; Bourdin et al., 2000; Mikelić et al., 2015). Therefore, the overall energy functional can be expressed as:

$$\psi(u,\Gamma,p)=\int_\Omega \psi(\varepsilon^e)d\Omega+\int_\Gamma G_c d\Omega+\int_\Omega \alpha p\cdot(\nabla\cdot u)d\Omega+\int_\Omega b\cdot u d\Omega+\int_{\partial\Omega} f\cdot u dS \tag{1}$$

where u and p represent the displacement field and fluid pressure, respectively. $\psi(\varepsilon^e)$ represents the elastic strain energy. G_c is the critical energy release rate, ∂ is the Biot coefficient, b is the body force, and f is the prescribed external force applied on the boundary.

The second term in equation (1), representing the fracture surface energy, can be rewritten in the domain integral as (Borden et al., 2012; Li and Zhou, 2019):

$$\int_\Gamma G_c dS\approx\int_\Omega G_c\gamma d\Omega=\int_\Omega\left(G_c\frac{\phi^2}{2l_0}+\frac{l_0}{2}|\nabla\phi|^2\right)d\Omega \tag{2}$$

The primary characteristic of the phase-field method is that it is driven by elastic energy. In this approach, we adopt an anisotropic formulation and eliminate unrealistic fracture modes (Miehe et al., 2010). Based on the spectral decomposition of the strain tensor, the elastic energy is decomposed into compressive and tensile components:

$$\varepsilon^{e\pm}=\sum_{a=1}^{d}\langle\varepsilon_a^e\rangle_\pm n_a\otimes n_a \tag{3}$$

here, ε^{e+} and ε^{e-} represent the tensile and compressive strain tensors, respectively. ε_a^e and n_a are the principal strain and its direction. The operators $\langle\cdot\rangle^+$ and $\langle\cdot\rangle^-$ are defined as $\langle\cdot\rangle^+=\max(\cdot,0))$ and $\langle\cdot\rangle^-=\min(\cdot,0)$.

Therefore, the tensile and compressive strains are used to construct the tensile and compressive parts of the elastic energy:

$$\psi^{\varepsilon\pm}(\varepsilon^e)=\frac{\lambda}{2}\langle tr(\varepsilon^e)\rangle_\pm^2+\mu tr[(\varepsilon^{e\pm})^2] \tag{4}$$

The elastic energy density is updated by combining the tensile and compressive energy components. It is assumed that the phase field only affects the tensile component of the elastic energy, while the compressive part is not considered (Miehe et al., 2010):

$$\psi^e(\varepsilon^e)=[(1-k)(1-\phi)^2+k]\psi^{\varepsilon+}(\varepsilon^e)+\psi^{\varepsilon-}(\varepsilon^e) \tag{5}$$

where $0<k\ll 1$ is a model parameter that increases numerical stability with the phase field tending to $\phi=1$.

2.2 Governing equations for phase field evolution

By substituting equations (2) and (4) into equation (1), we obtain the energy functional expression:

$$\begin{aligned}L=\psi(u,\Gamma)=&\int_\Omega\left\{[(1-k)(1-\phi)^2+k]\psi^{\varepsilon+}(\varepsilon^{e+})+\psi^{\varepsilon-}(\varepsilon^e)\right\}d\Omega\\&-\int_\Omega G_c\left(\frac{\phi^2}{2l_0}+\frac{l_0}{2}|\nabla\phi|^2\right)d\Omega+\int_\Omega\alpha p\cdot(\nabla\cdot u)d\Omega\\&+\int_\Omega b_i\cdot u_i d\Omega+\int_{\partial\Omega} f_i\cdot u_i dS.\end{aligned} \tag{6}$$

According to the variational minimization principle, by taking the variation of the energy functional$L$, the governing equations for the phase-field fracture model can be derived (Liu et al., 2020):

$$\begin{cases}\dfrac{\partial\sigma_{ij}}{\partial x_i}+\alpha I(\nabla p)+b_i=0\\ \left[\dfrac{2l_0(1-k)\psi^{\varepsilon+}}{G_c}+1\right]\phi-l_0^2\dfrac{\partial^2\phi}{\partial x_i^2}=\dfrac{2l_0(1-k)\psi^{\varepsilon+}}{G_c}\end{cases} \tag{7}$$

The effective stress tensor σ_{ij} is given by the following equation (Zhou et al., 2018):

$$\begin{aligned}\sigma_{ij}=&[(1-k)(1-\phi)^2+k]\left[\lambda\langle tr(\varepsilon)\rangle^+ I+2\mu\varepsilon^+\right]\\&+\lambda\langle tr(\varepsilon)\rangle^- I+2\mu\varepsilon^-\end{aligned} \tag{8}$$

To ensure that the fracture is irreparable and that the phase field is monotonically increasing, a history variable is introduced to prevent fracture healing during loading or unloading (Xia et al., 2017). It is defined as follows:

$$H(x,t)=\max_{s\in[0,t]}\psi^{\varepsilon+}\left[\varepsilon^e(x,s)\right] \tag{9}$$

By replacing the tensile strain energy density function $\psi^{\varepsilon+}$ in equation (9) with $H(x,t)$, the phase-field fracture equation can be rewritten as:

$$\begin{cases} \dfrac{\partial \sigma_{ij}}{\partial x_i} + \alpha I(\nabla p) + b_i = 0 \\ \left[\dfrac{2l_0(1-k)H}{G_c} + 1\right]\phi - l_0^2 \dfrac{\partial^2 \phi}{\partial x_i^2} = \dfrac{2l_0(1-k)H}{G_c} \end{cases} \tag{10}$$

2.3 Governing equation for the flow field

For the fluid field, the entire region is divided into three parts: the fractured zone, the transition zone, and the unfractured zone. Therefore, we introduce two phase-field thresholds, c_1 and c_2. When $\phi \le c_1$, it indicates the unfractured zone; when $\phi \ge c_2$, it indicates the fractured zone; and when $c_1 < \phi < c_2$, it indicates the transition zone. Li et al. proposed that the elastic and hydraulic parameters in the unfractured and fractured zones transition linearly in the transition zone(Liu et al., 2019). Based on this assumption, Lee et al. introduced two indicator functions, χ_R and χ_f which are defined as follows (Lee et al., 2016):

$$\chi_R = \begin{cases} 1, \phi \le c_1 \\ \frac{c_2-\phi}{c_2-c_1}, c_1 < \phi < c_2 \\ 0, \phi \ge c_2 \end{cases} \tag{11}$$

$$x_f = \begin{cases} 0, \phi \le c_1 \\ \frac{\phi-c_1}{c_2-c_1}, c_1 < \phi < c_2 \\ 1, \phi \ge c_2 \end{cases} \tag{12}$$

We apply Darcy's law to describe the fluid flow in porous media. The mass conservation for the entire region is given by the following equation (Zhou et al., 2020):

$$\rho S \frac{\partial p}{\partial t} - \nabla \cdot (\rho v) = q_m - \rho \alpha \chi_R \frac{\partial \varepsilon_{vol}}{\partial t} \tag{13}$$

here,$\rho, S, \upsilon, \varepsilon_{vol} and q_m$ represent the fluid density, storage coefficient, flow velocity, volumetric strain of the domain, and source term, respect tively. By defining ρ_R and ρ_f as the fluid densities in the unfractured and fractured zones, respectively, we obtain $\rho = \rho_R\chi_R + \rho_f\chi_f$. Similarly, $\alpha = \alpha_R\chi_R + \alpha_f\chi_f$ Assuming the Biot coefficient in the fractured zone $\alpha = 1$ we have $\alpha = \alpha_R\chi_R + \chi_f$, where α_R represents the Biot coefficient in the unfractured zone. In addition, ε_{vol} represents the volumetric strain.

The storage coefficient S can be expressed as (Zhuang et al., 2020):

$$S = \varphi c + \frac{(1-\alpha)(\alpha-\varphi)}{K_{vol}} \tag{14}$$

here,ϕ, c and K_{vol} represent the porosity, fluid compressibility coefficient, and bulk modulus, respectively. Similar to the previous expressions, the compressibility coefficient is given by: $c = c_R\chi_R + cf\chi_f$. The porosity $\varphi = \varphi R\chi_R + \varphi f\chi_f$, where in the fractured zone, $\varphi = 1$ thus $\varphi = \varphi R\chi_R + \chi_f$.

The Darcy velocity ϑ is defined as:

$$v = -\frac{K}{\mu}(\nabla p + \rho g) \tag{15}$$

where, K and μ represent the effective permeability and fluid viscosity, respectively. Similar to the previous expressions, the effective permeability is given by $K = KR\chi_R + K_f\chi_f$. The fluid viscosity is expressed as $\mu = \mu R\chi_R + \mu_f\chi_f$, where μ_R and μ_f are the fluid viscosities in the unfractured and fractured zones, respectively, and represents gravity.

3 Model validation

This section simulates the plate tension test with a single-edge notch and hydraulic fracturing problem, aiming to validate the phase-field calculation for fracture propagation caused by external force and fluid pressure.

3.1 Plate tension test with a single-edge notch

First, we validate fracture propagation in a notched square plate under tensile loading. The geometry and boundary conditions are shown in Fig.2(a). A displacement load is applied to the upper boundary, while the lower boundary is fixed. The material parameters are as follows: E=210GPa, ν=0.3, Gc=2700 N/m, and l0=1.5×$10^{-2}mm$. Fig.3 presents the load-displacement curve for the upper boundary of the plate, comparing it with the results obtained by Miehe et al. The load-displacement curve from this study closely matches that of (Miehe et al., 2010), demonstrating strong consistency between the two.

3.2 Experimental results from hydraulic fracturing

To further validate the feasibility of the model, we compare the phase-field simulation results with the hydraulic fracturing propagation experiments conducted on pre-notched specimens with circular holes. The original experiment was performed by Zhang et al., and subsequently Liu et al. (Zhang et al., 2017; Liu et al., 2018). validated the experimental results using a damage model. Fig. 2(b) illustrates the geometry and boundary conditions of the experiment, where the upper and right boundaries are stress boundaries, and water is injected into the specimen through a pre-drilled circular hole at the center. The relevant input parameters can be found in Liu's study. Moreover, as shown in Fig. 4, the fracture patterns obtained by using the phase field model are in line with those results in the experimental tests and damage simulations, further demonstrating the capability and practicability of the phase field model in simulating hydraulic fractures.

4 Numerical simulations and results discussions

To investigate fracture propagation within the "weak interlayer" during CO_2 geological sequestration, a model of layered

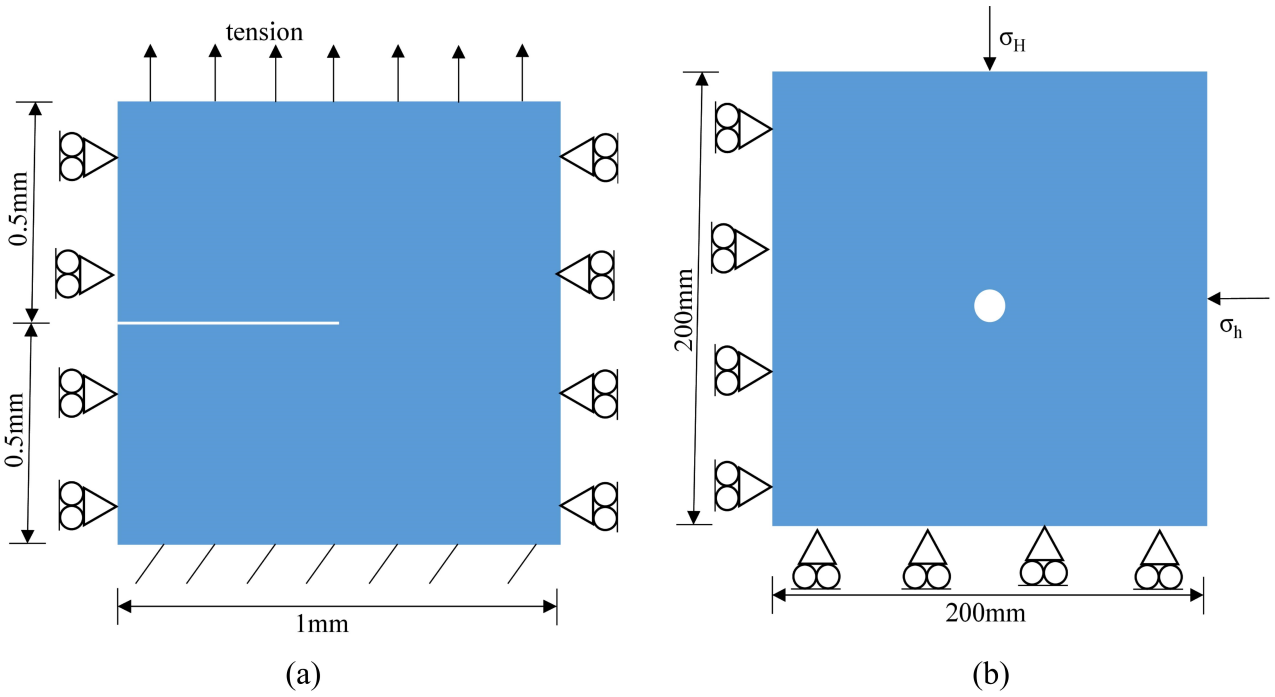

Fig. 2 Model geometric configuration for (a) plate tension test with single edge notch and (b)hydraulic fracturing experiments

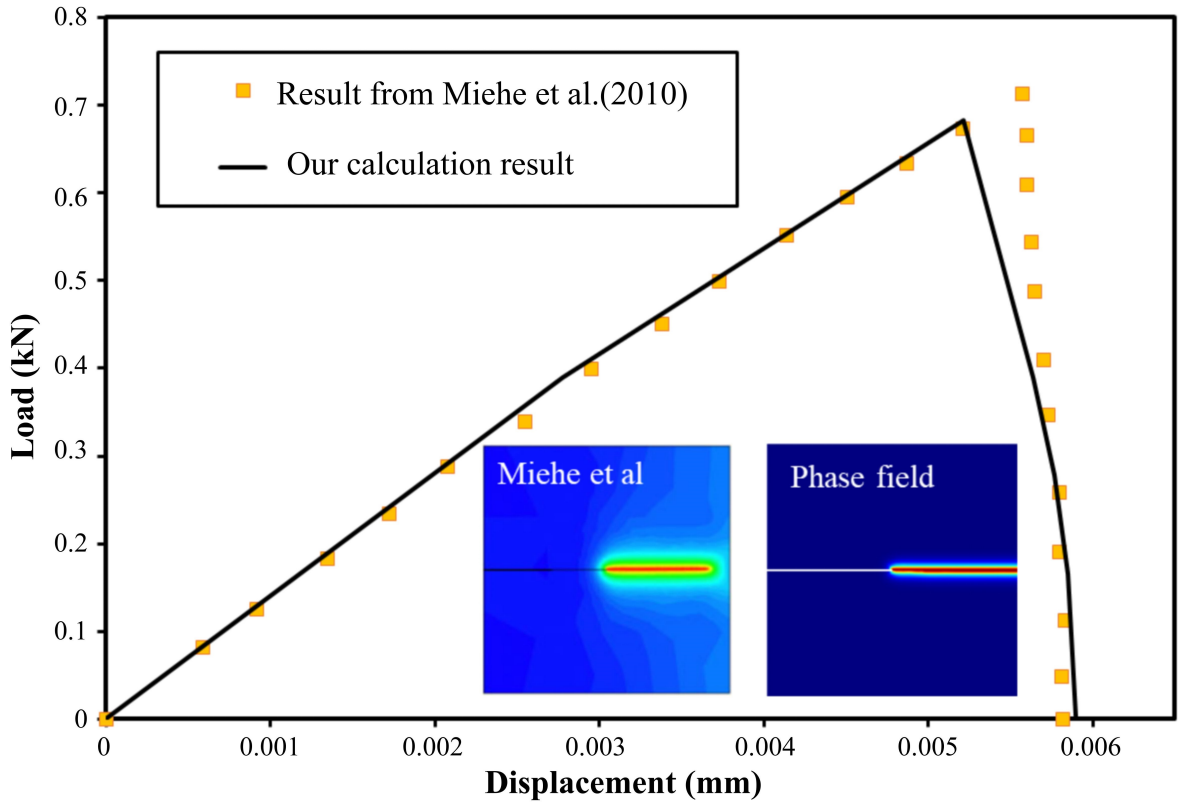

Fig. 3 Comparison of results from a square plate with an initial notch subjected to quasi-static tension loading

shale caprock is presented in Fig.5. This model has dimensions of 100m in length and 25m in width, comprising three "weak interlayer" and four matrix layers, each with different mechanical properties and permeabilities. The entire domain is discretized into triangular elements, with local mesh refinement applied to areas where fractures are likely to occur. The bottom boundary is a no-flow boundary, while the other permeable boundaries

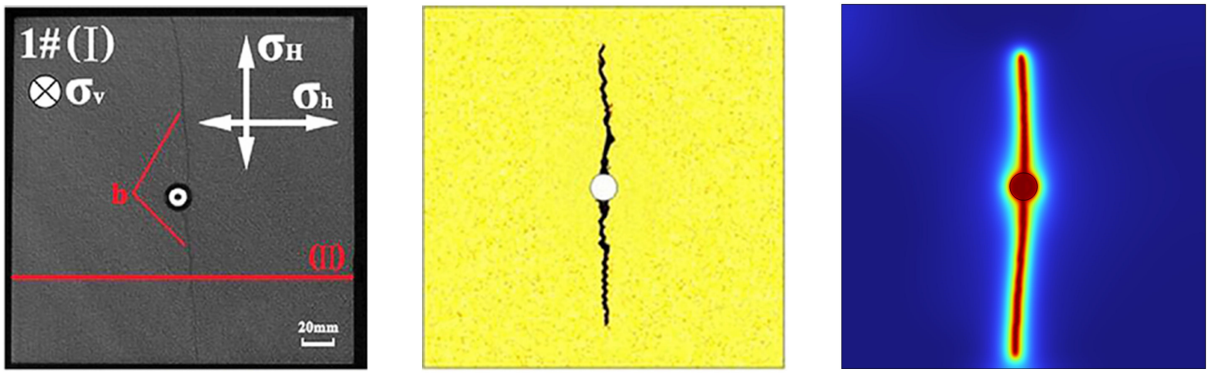

(a) (b) (c)

Fig. 4 Comparison between presented results and previous experimental and numerical results

are set to zero pressure. Vertical stress is applied at the top boundary, and horizontal stress is applied at the lateral boundaries, with the bottom boundary fixed in vertical displacement. The injection source is modeled as a red rectangular area at the bottom, with a flow rate of q_f=50$kg/(m^3 \cdot s)$. The red point at the top of the model is the displacement monitoring point, and the red point at the bottom is the pressure monitoring point. The input parameters for computation are listed in Table 1.

Tab. 1 Numerical simulation parameter

Parameter name	Value/Unit
Matrix elastic modulus E_0	60 GPa
Weak interlayer elastic modulus E_0'	30 GPa
Poisson's ratio ν	0.3
c_1	0.4
c_2	1.0
k	1×10^{-9}

4.1 CO_2 migration behavior in layered shale caprock

This study investigates CO_2 migration behavior under three in-situ stress conditions (12 MPa, 15 MPa, and 20 MPa) with a constant injection rate of qf=50$kg/(m^3 \cdot s)$. Fig. 7(a)-(d) depicts fracture propagation paths under 12 MPa in-situ stress. At 7.5 *s*, the fracture vertically penetrates the matrix and reaches the first "weak interlayer". Due to the higher permeability of "weak interlayer" compared to the matrix, CO_2 preferentially migrates and diffuses along this layer, causing the fracture trajectory to deflect horizontally. By 10 *s*, the fracture extends significantly along the "weak interlayer", forming a characteristic T-shaped fracture within the layered shale caprock. Fig. 7(g)-(h) demonstrate that under 15 MPa in-situ stress, fractures similarly develop T-shaped geometries. However, at 10s, the fracture propagation is restricted to the first "weak interlayer", indicating that elevated in-situ stress still inhibits fracture propagation. Under 20 MPa in-situ stress (Fig.7(i)-(l)), while fractures maintain T-shaped configurations, their propagation dynamics exhibit distinct differences. At 50 *s*, the fracture penetrates the first "weak interlayer" and continues vertical propagation, likely because increased in-situ stress reduces the CO_2 pressure dissipation rate, maintaining sufficient driving pressure for vertical extension. By 100 *s*, the fracture reaches the second "weak interlayer", where it deflects and resumes horizontal propagation.

Fig.8 further presents the CO_2 pressure evolution within the caprock under three in-situ stress conditions. All three curves display a consistent pattern of rapid pressure buildup followed by a gradual decline. Notably, the fracture initiation pressure increases with higher in-situ stress, rising from 32 MPa to 42 MPa. Taking the 20 MPa condition as a representative case, the pressure evolution can be divided into four stages:

(i) 0-(a) Pressure accumulation stage: CO_2 pressure rapidly accumulates until it reaches the fracture initiation threshold of the caprock matrix, marking the onset of fracture propagation.

(ii) (a)-(b) Fracture propagation stage: The fracture propagates steadily through the matrix until encountering the first "weak interlayer". A sharp pressure drop occurs at this stage due to rapid fluid pressure dissipation through the highly permeable "weak interlayer".

(iii) (b)-(c) Secondary interlayer penetration stage: After passing through the first "weak interlayer", partial CO_2 migration occurs along this layer, leading to significantly slower fracture propagation rates during this stage.

(iiii) (c)-(d) Stable horizontal propagation stage: Upon reaching the second "weak interlayer", the CO_2 pressure shows a minor reduction.

At this point, the residual CO_2 pressure becomes insufficient to sustain further vertical propagation. While pressure gradually re-accumulates, the extensive existing fracture network limits the efficiency of pressure buildup. Consequently, the fracture transitions to horizontal propagation along the "weak interlayer" until reaching stabilization.

4.2 Sensitivity analysis

4.2.1 Effect of lateral stress

In the previous section, lateral and vertical stresses were assumed to be equal. However, under realistic in-situ conditions, lateral stress is ypically lower than the vertical stress. As demonstrated by Zhou's simulation results, reducing lateral

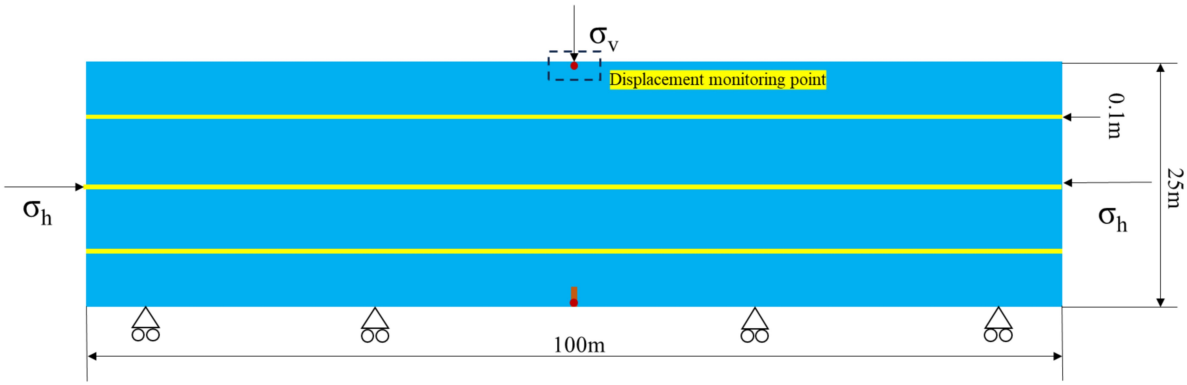

Fig. 5 Geometry and boundary conditions of layered shale caprock

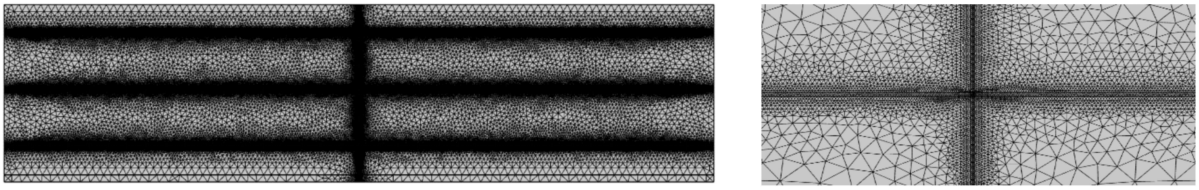

(a) (b)

Fig. 6 Mesh used for simulation (a) Entire mesh, (b) Magnified local mesh

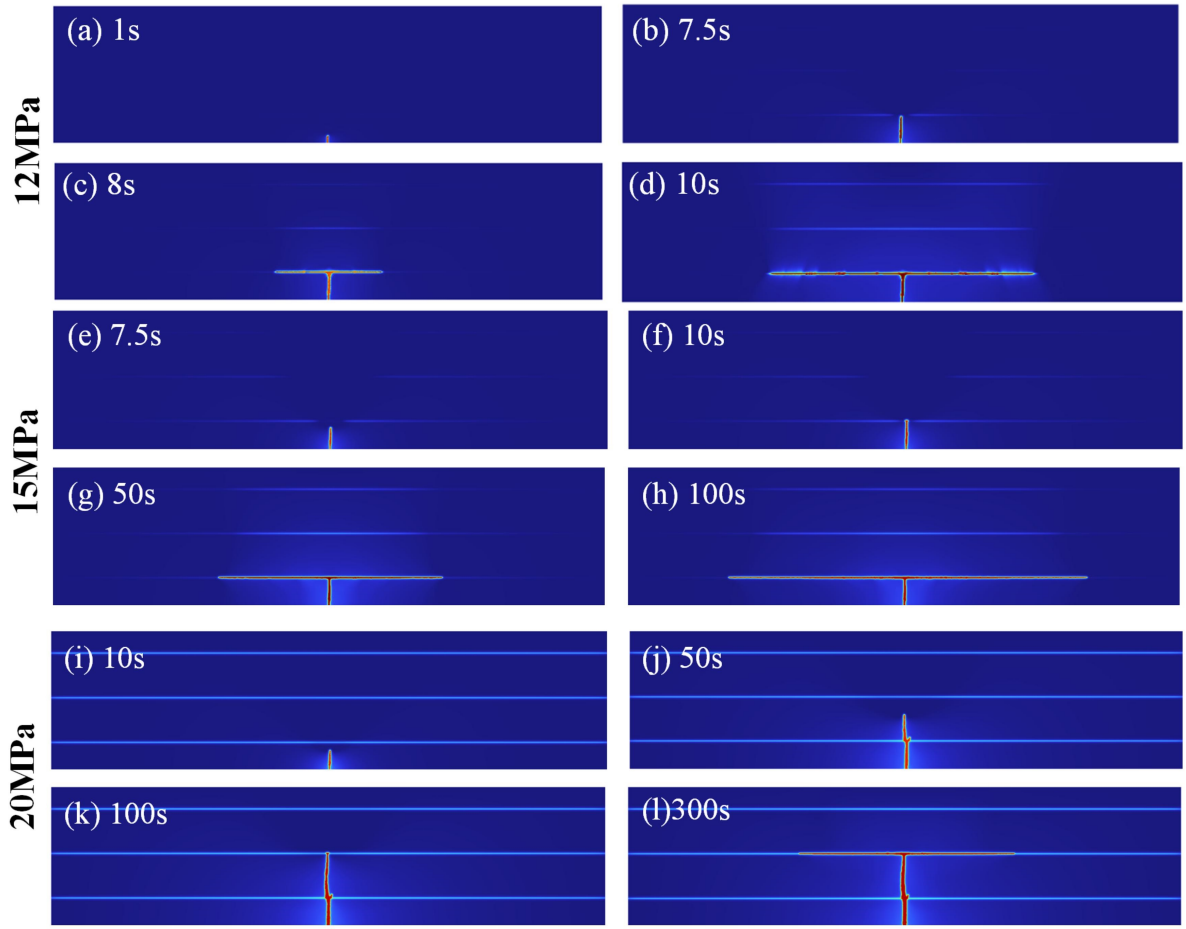

Fig. 7 Comparison of fracture propagation paths under in-situ stresses of 12 MPa, 15 MPa and 20 MPa

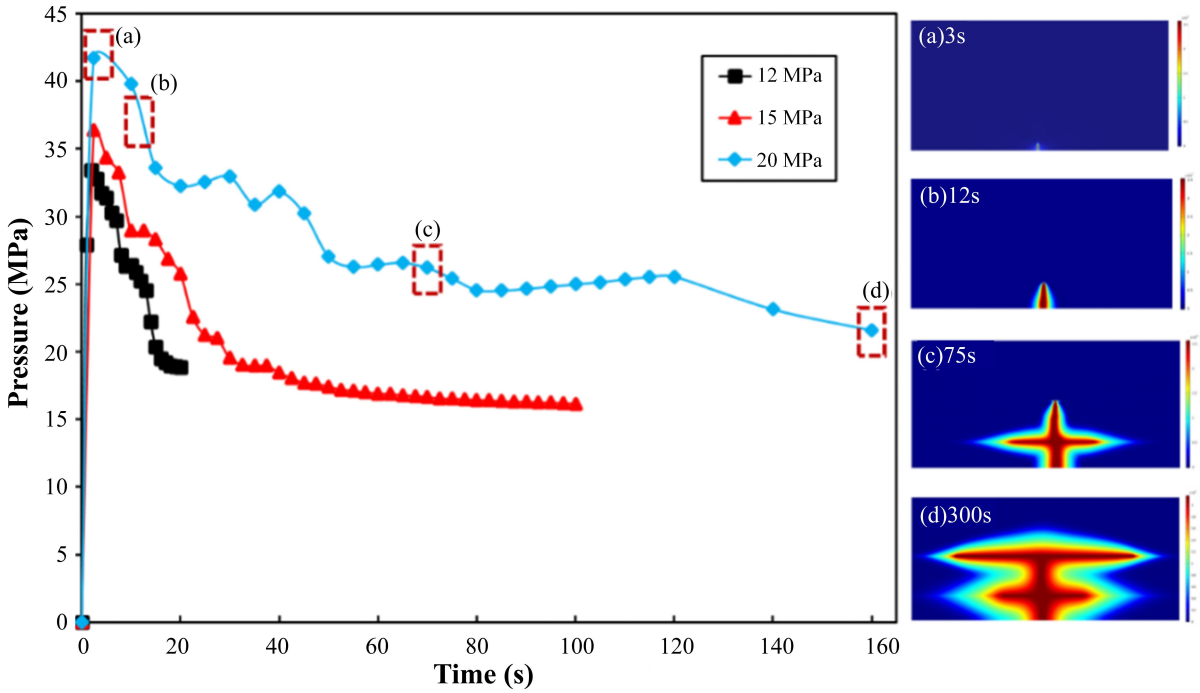

Fig. 8 Comparison of CO_2 pressure evolution under in-situ stress of 12 MPa, 15 MPa and 20 MPa

stress tends to promote vertical fracture propagation (Zhou et al., 2020). Consequently, assuming equal lateral and vertical stresses could lead to an overestimation of the caprock's sealing capacity. In this section, we maintain a constant vertical stress of 15 MPa while reducing the lateral stress from 15 MPa to 12 MPa to systematically compare the CO_2 migration behavior within the layered shale caprock.

Fig. 9(a)-(f) compares fracture propagation paths within the layered shale caprock under two stress conditions:

(i) vertical stress of 15 MPa with equal lateral stress (15 MPa),

(ii) vertical stress of 15 MPa with reduced lateral stress (12 MPa).

At 8 *s*, both conditions show similar fracture advancement towards the first "weak interlayer". However, a significant divergence emerges subsequently. Under the 12 MPa lateral stress condition, fractures penetrate the second "weak interlayer" by 11.6 *s* and ultimately breach the third interlayer, reaching the top of the caprock by 20 *s*. In contrast, under 15 MPa lateral stress, fractures only deflect at the first "weak interlayer" by 20 *s*, forming characteristic T-shaped propagation.

Fig.10 further presents the corresponding CO_2 pressure evolution. Both conditions demonstrate similar CO_2 pressure trends, featuring a rapid increase followed by gradual decline. Notably, due to the reducing lateral stress from 15 CO_2 to 12 MPa, fracture initiation pressure decreases from 37 MPa to 32 MPa. Detailed analysis of pressure distribution at three "weak interlayer" under 12 MPa lateral stress (Fig.10a-c) reveals minimal CO_2 migration along these "weak interlayer". This observation indicates that reduced lateral stress suppresses horizontal CO_2 migration, thereby maintaining consistent pressure decline rates throughout the fracture propagation process.

4.2.2 Effect of permeability differences in "weak interlayer"

As discussed earlier, the high permeability of the "weak interlayer" is critical for horizontal CO_2 migration within layered shale caprock. However, due to variations in deposition patterns within layered shale caprock, the permeability of the "weak interlayer" may be relatively lower. In the previous cases, the permeability of the "weak interlayer" was set to be two orders of magnitude higher than the matrix, which may have overestimated the pressure dissipation capability of the "weak interlayer" Therefore, in this section, the initial permeability of the "weak interlayer" is reduced to $1 \times 10^{-15} m^2$.

Fig. 11 compares fracture propagation paths in "weak interlayer" with permeabilities of $1 \times 10^{-14} m^2$ and $1 \times 10^{-15} m^2$. The results demonstrate that reduced permeability ($1 \times 10^{-15} m^2$) produces fracture behavior is similar to that observed under decreased lateral stress (12 MPa), where fractures vertically penetrate "weak interlayer" without deflection. Specifically, fractures breach the second and third "weak interlayer" at 18 *s* and 50 *s* respectively, ultimately reaching the top of the caprock (Fig.11d-f).

Fig.12 presents the pressure evolution for the "weak interlayer" with permeabilities of $1 \times 10^{-14} m^2$ and $1 \times 10^{-15} m^2$. The results indicate that the pressure evolution trends under both conditions are similar, with no significant difference in fracture initiation pressure. However, the reduced permeability of the "weak interlayer" ($1 \times 10^{-15} m^2$) hinders gas pressure dissipation. Consequently, the CO_2 pressure declines more gradually from the peak to point (a). When CO_2 migrates to the first "weak interlayer", the pressure decreases by only 4 MPa before transitioning to an upward trend, suggesting that the pressure dissipation efficiency of the "weak interlayer" cannot

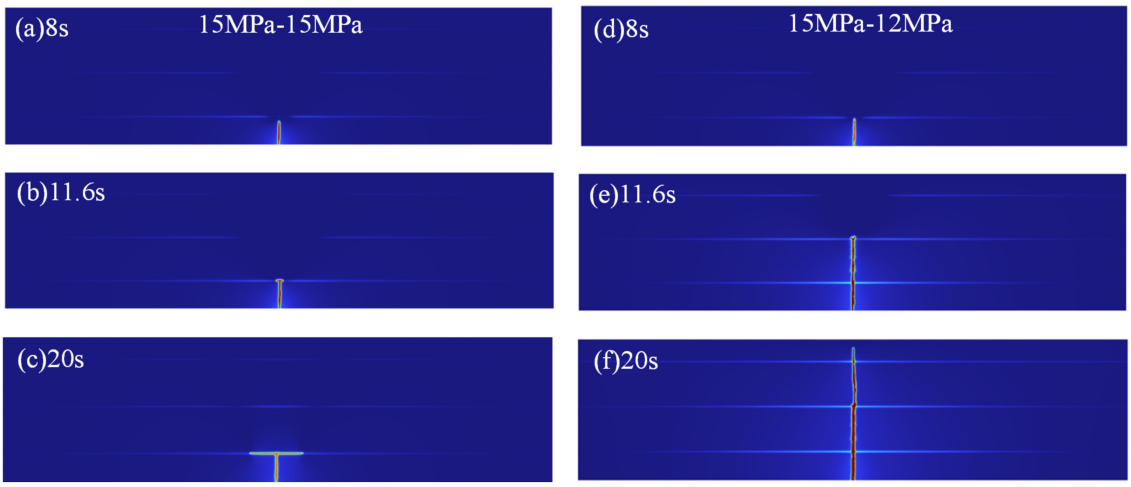

Fig. 9 Comparison of fracture propagation paths under lateral stresses of 15 MPa and 12 MPa

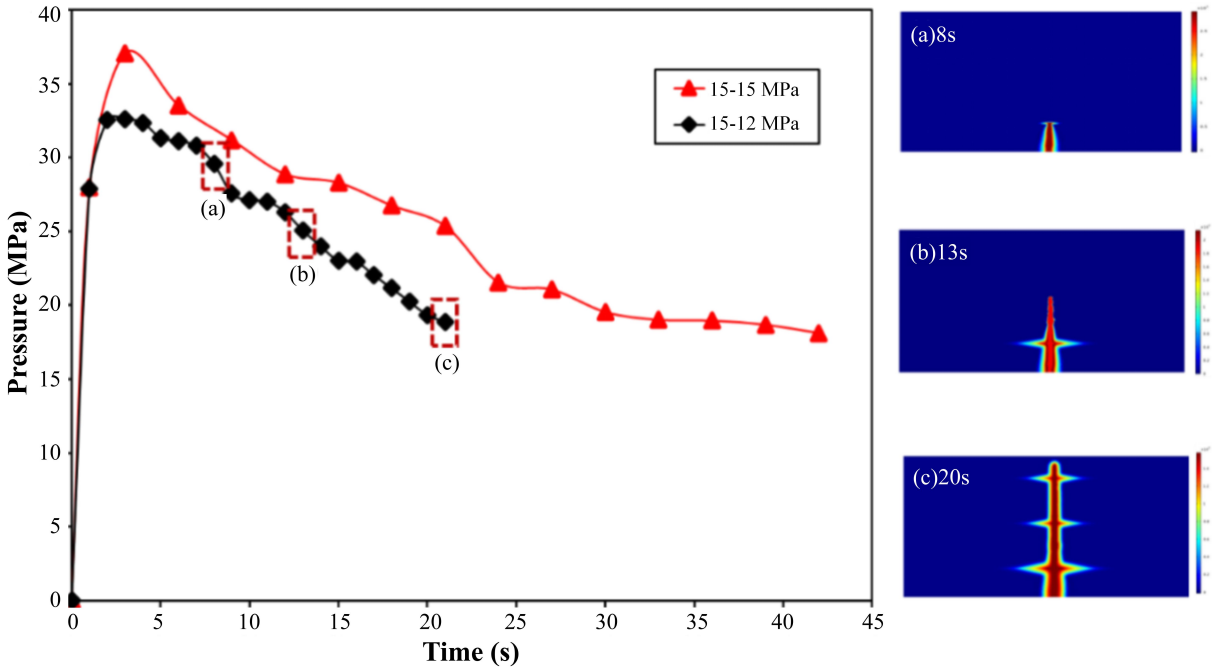

Fig. 10 Comparison of CO_2 pressure evolution under lateral stresses of 15 MPa and 12 MPa

keep up with the CO_2 injection rate. This also explains the slow pressure increase observed during the final stable propagation stage (b)–(c).

4.2.3 Effect of injection rate

The aforementioned study reveals that elevated in-situ stress restricts the horizontal dissipation of CO_2, while rapid pressure accumulation promotes vertical fracture initiation in layered shale caprock, thereby facilitating CO_2 leakage. To mitigate this risk, the injection rate was reduced to 25 $kg/(m^3 \cdot s)$ under an in-situ stress of 20 MPa, and its effect on CO_2 migration behavior was systematically investigated.

Fig. 13 compares fracture propagation paths under different injection rates: $q_f = 50kg/(m^3 \cdot s)$ and 25 $kg/(m^3 \cdot s)$. While both conditions exhibit T-shaped fracture patterns, distinct temporal differences emerge in interlayer penetration behavior. At $q_f = 25kg/(m^3 \cdot s)$, fractures deflect immediately upon reaching the first "weak interlayer" at 24 s. At $q_f = 50kg/(m^3 \cdot s)$, fractures penetrate the first interlayer and only deflect at the second "weak interlayer" at 100 s.

Fig.14 shows the pressure evolution under injection rates of $q_f = 25kg/(m^3 \cdot s)$ and $q_f = 50kg/(m^3 \cdot s)$. The results reveal that the two curves exhibit similar evolutionary trends. However, under the lower injection rate $q_f = 25kg/(m^3 \cdot s)$), the pressure drops rapidly once the fracture propagates to the first "weak interlayer". The minimum pressure reached in this case is 3 MPa lower than that under $q_f = 50kg/(m^3 \cdot s)$. Additionally, a longer pressure accumulation period is required to restore the pressure conditions necessary for further fracture propagation. This demonstrates that the pressure accumulation rate under the lower injection rate is insufficient to compensate for the

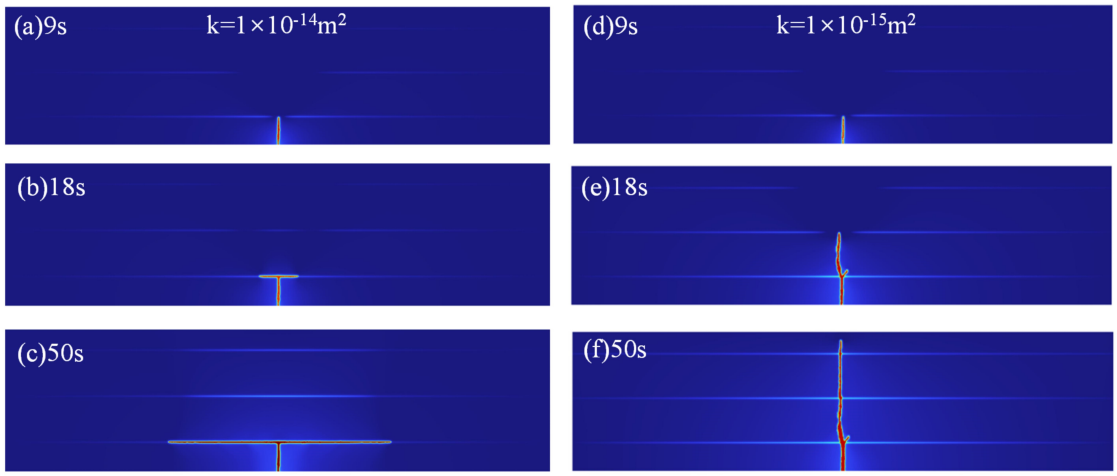

Fig. 11 Comparison of fracture propagation paths under the "weak interlayer" permeability of $1 \times 10^{-15} m^2$ and $1 \times 10^{-14} m^2$

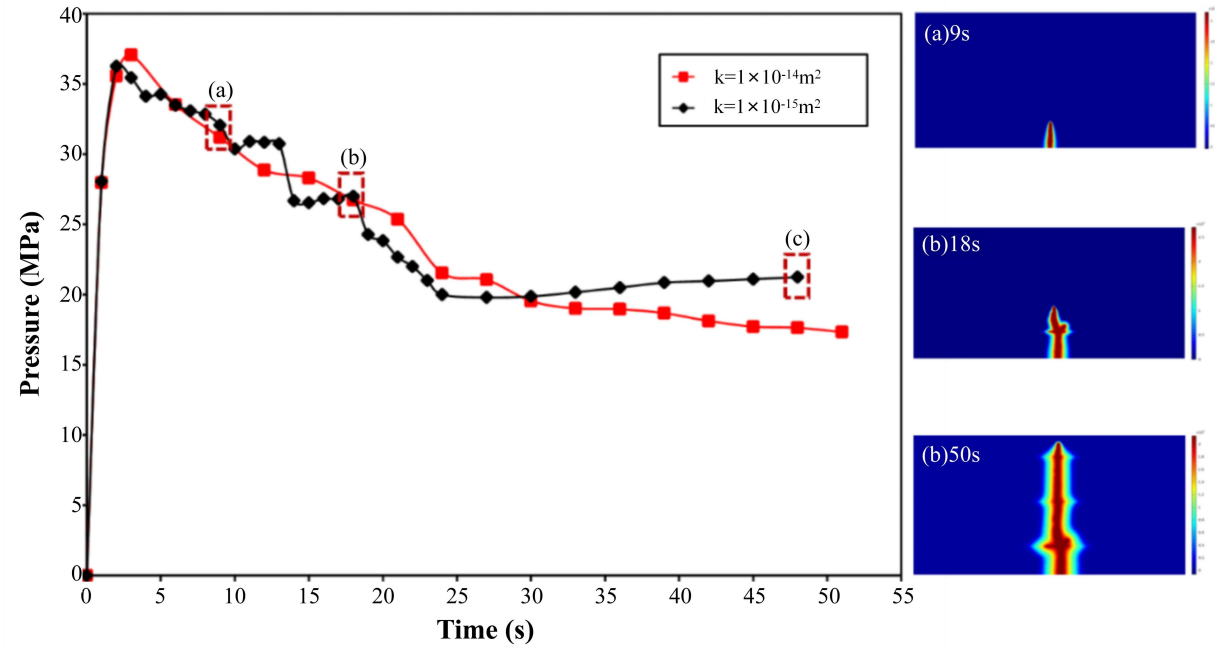

Fig. 12 Comparison of CO_2 pressure evolution under the "weak interlayer" permeability $1 \times 10^{-15} m^2$ and $1 \times 10^{-14} m^2$

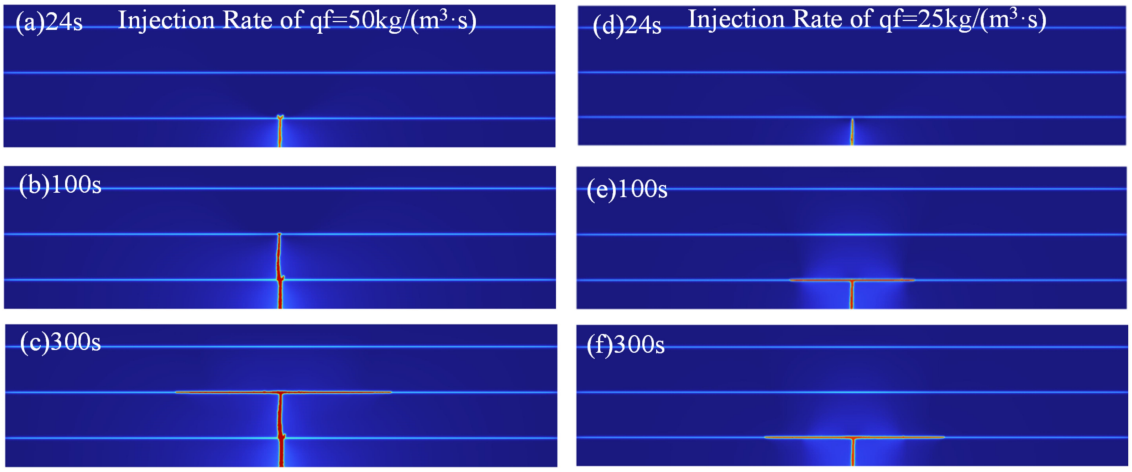

Fig. 13 Comparison of fracture propagation paths under the injection rate $q_f = 25kg/(m^3 \cdot s)$ and $q_f = 50kg/(m^3 \cdot s)$

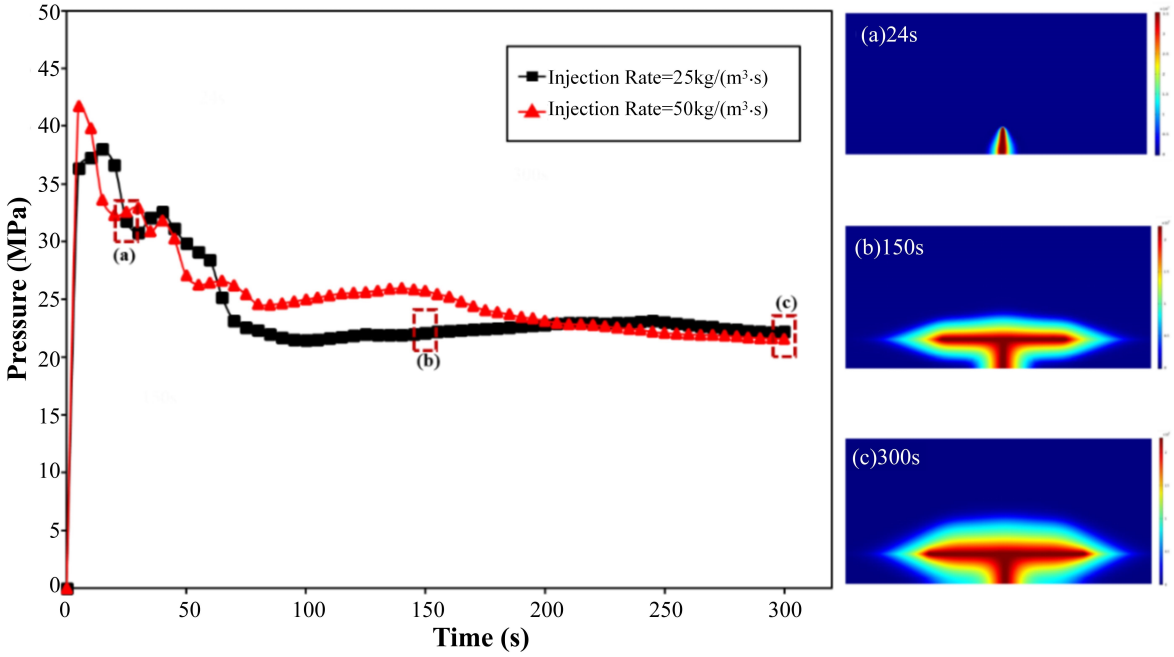

Fig. 14 Comparison of CO_2 pressure evolution under the injection rate $q_f = 25kg/(m^3 \cdot s)$ and $q_f = 50kg/(m^3 \cdot s)$

Tab. 2 Summary of numerical simulation results

Case No	S_v (MPa)	S_h (MPa)	Matrix permeability (m^2)	"weak interlayer" permeability (m^2)	Injection rate ($kg/(m^3 \cdot s)$)	Propagation mode	Fracture pressure (MPa)
a	12	12	1×10^{-16}	1×10^{-14}	50	Horizontal migration	32
b	15	15	1×10^{-16}	1×10^{-14}	50	Horizontal migration	37
c	20	20	1×10^{-16}	1×10^{-14}	50	Concurrent	42
d	15	12	1×10^{-16}	1×10^{-14}	50	Horizontal migration	32
e	20	20	1×10^{-16}	1×10^{-14}	25	Vertical migration	38
f	15	15	1×10^{-16}	1×10^{-15}	50	Vertical migration	37

pressure dissipation rate in the "weak interlayer".

4.3 Evaluation of CO_2 geological sequestration in layered shale caprock with "weak interlayer"

As presented in Table 2, numerical simulations reveal that the pressure required for vertical CO_2 migration through the layered shale caprock is significantly higher than that needed for lateral migration along the "weak interlayer". Highly permeable "weak interlayer" facilitate rapid CO_2 pressure dissipation, thereby preventing the buildup of sufficient pressure for vertical migration. This demonstrates that "weak interlayer" plays a crucially positive role in the sealing integrity of layered shale caprocks during CO_2 storage. The fracture initiation pressure of the caprock increases with higher geostatic stress. However, elevated stress conditions simultaneously restrict horizontal CO_2 diffusion along the "weak interlayer". Under prolonged CO_2 accumulation, this stress configuration makes vertical leakage more likely to occur. This tendency is further exacerbated by reductions in lateral stress and increases in "weak interlayer" permeability, which not only promote vertical leakage but also dramatically shorten the timescale for CO_2 breakthrough through the caprock. These results confirm that the primary mechanism for vertical CO_2 leakage stems from the pressure imbalance, where the "weak interlayer" dissipation rate cannot match the fluid injection rate, leading to excessive pressure buildup. Therefore, when necessary, implementing intermittent CO_2 injection or reducing the injection rate can effectively decrease CO_2 accumulation. This allows gradual diffusion through the caprock, preventing pressure buildup sufficient to drive vertical CO_2 leakage. Such operational modifications significantly enhance the safety of geological CO_2 storage.

5 Conclusions

This study proposes a method using the phase-field approach to simulate the CO_2 migration behavior in layered shale caprock containing "weak interlayer". The effects of different in-situ stress conditions, reduced lateral stress, decreased "weak interlayer" permeability, and reduced injection rate on CO_2 migration behaviors were analyzed. Additionally, various factors

were comprehensively assessed to determine the optimal and unfavorable storage conditions for layered shale caprock. The following conclusions can be obtained:

This model effectively captures fracture evolution and CO_2 migration patterns in layered caprocks during geological sequestration of CO_2. The findings establish that low-permeability layered shale caprock containing "weak interlayer" should be prioritized as primary sealing units for geological sequestration of CO_2.

Under conditions of high in-situ stress, internal layers are more likely to be vertically penetrated between them at high fracture initiation pressures, thus forming connected flow pathways. Notably, sufficient CO_2 accumulation is a necessary precondition for the fractures to still expand under high in-situ stress.

"weak interlayer" will release the CO_2 accumulation pressure, creating a T-shaped migration pattern. If the lateral stress is relatively low, this stress-buffering effect will be replaced by vertical fracture extension. Also, vertical fracture extension is found to be negatively correlated with the permeability of the "weak interlayer". Finally, the injection rate significantly increases the efficiency of interlayer fracture penetration.

Limitations

This study investigates fracture activation in layered caprock and associated CO_2 migration, processes governed by both physical property changes from supercritical state to gaseous state (phase transition) and chemical reactions between CO_2 and rock minerals. Several limitations must be acknowledged. The current model is built upon an idealized framework that primarily considers changes in CO_2 viscosity and density during phase transition, while explicitly omitting chemical interactions between CO_2 and reservoir minerals. This omission may limit the model's capacity to accurately represent long-term containment behavior. To address these constraints, future research will integrate multiphysics simulations that concurrently capture the coupled physicochemical interactions between CO_2 and geological formations. Furthermore, machine learning techniques will be employed to systematically explore key parameter combinations and their nonlinear effects on containment security, thereby enhancing the predictive transferability of the results to practical engineering contexts. Finally, we will seek collaboration with ongoing industrial carbon storage projects to incorporate representative field data for model inversion and calibration. Collectively, these steps are designed to improve the generalizability and practical utility of the findings, ultimately contributing to the design of safer and more effective CO_{22} storage systems as part of global carbon mitigation efforts.

Acknowledgements

The authors acknowledge the financial support from the National Natural Science Foundation of China under Grant No. 42372296 and No. 42202286, the China Postdoctoral Science Foundation under Grant No. 2023M730916.

Conflict of interest

The authors declare no competing interest.

References

Bourdin B, Francfort G A, Marigo J-J. 2000. Numerical experiments in revisited brittle fracture. *Journal of the Mechanics and Physics of Solids*, **48**:797–826. doi:10.1016/S0022-5096(99)00028-9.

Borden M J, Verhoosel C V, Scott M A, et al. 2012. A phase-field description of dynamic brittle fracture. *Computer Methods in Applied Mechanics and Engineering*, **217–220**:77–95. doi:10.1016/j.cma.2012.01.008.

Chen B, Qi L, Tan Y, Liu W, Zhang Y. 2024. Caprock sealing integrity and key indicators of CO_2 geological storage considering the effect of hydraulic-mechanical coupling: X field in the Bohai Bay Basin, China. *Engineering Geology*, **342**:107741. doi:10.1016/j.enggeo.2024.107741.

Francfort G A, Marigo J-J. 1998. Revisiting brittle fracture as an energy minimization problem. *Journal of the Mechanics and Physics of Solids*, **46**:1319–1342. doi:10.1016/S0022-5096(98)00034-9.

Kaldi J, Daniel R, Tenthorey E, et al. 2013. Containment of CO_2 in CCS: Role of caprocks and faults. *Energy Procedia*, **37**:5403–5410. doi:10.1016/j.egypro.2013.06.458.

Lee J, Min K-B, Rutqvist J. 2013. Ground heaving and leakage analysis for sequestration of CO_2 in geological media considering fractures in caprock. *Energy Procedia*, **37**:4504–4510. doi:10.1016/j.egypro.2013.06.356.

Lee S, Wheeler M F, Wick T. 2016. Pressure and fluid-driven fracture propagation in porous media using an adaptive finite element phase field model. *Computer Methods in Applied Mechanics and Engineering*, **305**:111–132. doi:10.1016/j.cma.2016.02.037.

Li K, Zhou S. 2019. Numerical investigation of multizone hydraulic fracture propagation in porous media: New insights from a phase field method. *Journal of Natural Gas Science and Engineering*, **66**:42–59. doi:10.1016/j.jngse.2019.03.018.

Liu J, Kai Y, Yi X, et al. 2019. Study on fracture behavior of bedded shale in three-point-bending test based on hybrid phase-field modelling. *Theoretical and Applied Fracture Mechanics*, **104**:102382. doi:10.1016/j.tafmec.2019.102382.

Liu J, Liang X, Xue Y, et al. 2020. Investigation on crack initiation and propagation in hydraulic fracturing of bedded shale by hybrid phase-field modeling. *Theoretical and Applied Fracture Mechanics*, **108**:102651. doi:10.1016/j.tafmec.2020.102651.

Liu J, Xue Y, Chen W, et al. 2021. Variational phase-field model based on lower-dimensional interfacial element in FEM framework for investigating fracture behavior in layered rocks. *Engineering Fracture Mechanics*, **255**:107962. doi:10.1016/j.engfracmech.2021.107962.

Liu J, Xue Y, Zhang Y, et al. 2022. Phase-field modeling for dynamic cracking behavior in bedded shale. *Theoretical and Applied Fracture Mechanics*, **121**:103480. doi:10.1016/j.tafmec.2022.103480.

Liu L, Zhu W, Wei C, et al. 2018. Microcrack-based geomechanical modeling of rock-gas interaction during supercritical CO_2 fracturing. *Journal of Petroleum Science and Engineering*, **164**:91–102. doi:10.1016/j.petrol.2018.01.049.

Mikelić A, Wheeler MF, Wick T. 2015. A phase-field method for propagating fluid-filled fractures coupled to a surrounding porous medium. *SIAM Journal on Multiscale Modeling*

& Simulation, **13**(1):367–398. doi:10.1137/140967118.

Mikelić A, Wheeler MF, Wick T. 2015. A quasistatic phase field approach to pressurized fractures. *Nonlinearity*, **28**(5):1371–1399. doi:10.1088/0951-7715/28/5/1371.

Miehe C, Hofacker M, Welschinger F. 2010. A phase field model for rate-independent crack propagation: Robust algorithmic implementation based on operator splits. *Computer Methods in Applied Mechanics and Engineering*, **199**:2765–2778. doi:10.1016/j.cma.2010.04.011.

Newell P, Martinez M J. 2020. Numerical assessment of fault impact on caprock seals during CO_2 sequestration. *International Journal of Greenhouse Gas Control*, **94**:102890. doi:10.1016/j.ijggc.2019.102890.

Onoja MU, Williams JDO, Vosper H, et al. 2019. Effect of sedimentary heterogeneities in the sealing formation on predictive analysis of geological CO_2 storage. *International Journal of Greenhouse Gas Control*, **82**:229–243. doi:10.1016/j.ijggc.2019.01.013.

Span R, Wagner W. 1996. A new equation of state for carbon dioxide covering the fluid region from the triple-point temperature to 1100 K at pressures up to 800 MPa. *Journal of Physical and Chemical Reference Data*, **25**(6):1509–1596. doi:10.1063/1.555991.

Rutqvist J, Vasco DW, Myer L. 2010. Coupled reservoir-geomechanical analysis of CO_2 injection and ground deformations at In Salah, Algeria. *International Journal of Greenhouse Gas Control*, **4**:225–230. doi:10.1016/j.ijggc.2009.10.017.

Vilarrasa V, Bolster D, Olivella S, Carrera J. 2010. Coupled hydromechanical modeling of CO_2 sequestration in deep saline aquifers. *International Journal of Greenhouse Gas Control*, **4**:910–919. doi:10.1016/j.ijggc.2010.06.006.

Vilarrasa V, Olivella S, Carrera J. 2011. Geomechanical stability of the caprock during CO_2 sequestration in deep saline aquifers. *Energy Procedia*, **4**:5306–5313. doi:10.1016/j.egypro.2011.02.511.

Wang JG, Wang H. 2018. Sealing efficiency analysis for shallow-layer caprocks in CO_2 geological storage. *Environmental Earth Sciences*, **77**:738. doi:10.1007/s12665-018-7924-2.

Wang J G, Ju Y, Gao F, et al. 2015. Effect of CO_2 sorption-induced anisotropic swelling on caprock sealing efficiency. *Journal of Cleaner Production*, **103**:685–695. doi:10.1016/j.jclepro.2014.08.024.

Wang JG, Peng Y. 2014. Numerical modeling for the combined effects of two-phase flow, deformation, gas diffusion and CO_2 sorption on caprock sealing efficiency. *Journal of Geochemical Exploration*, **144**:154–167. doi:10.1016/j.gexplo.2013.12.011.

Xia L, Yvonnet J, Ghabezloo S. 2017. Phase field modeling of hydraulic fracturing with interfacial damage in highly heterogeneous fluid-saturated porous media. *Engineering Fracture Mechanics*, **186**:158–180. doi:10.1016/j.engfracmech.2017.10.005.

Yamamoto S, Miyoshi S, Sato S, et al. 2013. Study on geomechanical stability of the aquifer-caprock system during CO_2 sequestration by coupled hydromechanical modelling. *Energy Procedia*, **37**:3989–3996. doi:10.1016/j.egypro.2013.06.298.

Zeng Q, Bo L, Liu W, et al. 2023. An investigation of hydraulic fracture propagation in multi-layered formation via the phase field method. *Computers and Geotechnics*, **156**:105258. doi:10.1016/j.compgeo.2023.105258.

Zhou S, Zhuang X, Rabczuk T. 2018. A phase-field modeling approach of fracture propagation in poroelastic media. *Engineering Geology*, **240**:189–203. doi:10.1016/j.enggeo.2018.04.008.

Zhou S, Rabczuk T, Zhuang X. 2018. Phase field modeling of quasi-static and dynamic crack propagation: COMSOL implementation and case studies. *Advances in Engineering Software*, **122**:31–49. doi:10.1016/j.advengsoft.2018.03.012.

Zhou S, Zhuang X, Rabczuk T. 2020. Phase field method for quasi-static hydro-fracture in porous media under stress boundary condition considering the effect of initial stress field. *Theoretical and Applied Fracture Mechanics*, **107**:102523. doi:10.1016/j.tafmec.2020.102523.

Zhuang X, Zhou S, Sheng M, et al. 2020. On the hydraulic fracturing in naturally-layered porous media using the phase field method. *Engineering Geology*, **266**:105306. doi:10.1016/j.enggeo.2019.105306.

Zhang X, Lu Y, Tang J, et al. 2017. Experimental study on fracture initiation and propagation in shale using supercritical carbon dioxide fracturing. *Fuel*, **190**:370–378. doi:10.1016/j.fuel.2016.10.120.

IPCC. 2007. Climate Change 2007: Mitigation of Climate Change. Contribution of Working Group III to the Fourth Assessment Report of the Intergovernmental Panel on Climate Change.

IPCC. 2014. Climate Change 2014: Mitigation of Climate Change. Contribution of Working Group III to the Fifth Assessment Report of the Intergovernmental Panel on Climate Change.